Desalination and Water Treatment
www.deswater.com
doi: 10.5004/dwt.2023.29640

297 (2023) 1–16
June

Comparison of high-pressure and low-pressure fouling detectors at a full-scale seawater reverse osmosis desalination plant

Jishan Wu[a], Dian Tanuwidjaja[a,b], Gregory R. Guillen[a], Catalina Marambio-Jones[a], Robert Cheng[b], Arian Edalat[c], Eric M.V. Hoek[a,*]

[a]*Department of Civil and Environmental Engineering, California NanoSystems Institute and Institute for the Environment and Sustainability, University of California, Los Angeles, CA 90095, USA, Tel.: +1.310.794.7124; Fax: +1.310.206.2222; emails: emvhoek@ucla.edu (E.M.V. Hoek), wujishan123@g.ucla.edu (J. Wu), dianh2o@gmail.com (D. Tanuwidjaja), gguillen@dudek.com (G.R. Guillen), cmarambi@ucla.edu (C. Marambio-Jones)*
[b]*Long Beach Water Department, Long Beach, CA 90806, USA, email: RCheng@cvwd.org*
[c]*Pacifica Water Solutions, Northridge, CA 91326, USA, email: arian@pws-water.com*

Received 12 December 2022; Accepted 12 May 2023

ABSTRACT

In an attempt to better understand and control seawater reverse osmosis (RO) membrane fouling, low-pressure (LPFD) and high-pressure fouling detectors (HPFD) were employed in an *ex situ*, side-stream configuration at a full-scale seawater desalination plant. These fouling detectors contained flat-sheet membrane and spacer materials extracted from the membrane modules installed at the plant. The high-pressure fouling detectors reasonably replicated full-scale plant permeate quality, permeate flux, and differential pressure, whereas low-pressure fouling detectors could only simulate differential pressure. When evaluating different pre-treatments, it was observed that activated carbon and chlorine dioxide (after chlorination, microfiltration and dechlorination) to be effective at preventing RO membrane fouling, whereas chlorination, microfiltration and dechlorination and the same sequence followed by ultraviolet irradiation were less effective. Accelerated fouling was found when dosing both colloidal and dissolved nutrients, but the colloidal nutrient caused more severe fouling through a combination of colloidal cake layer formation in addition to biofilm formation and growth. In some cases, differential pressure may be an adequate early warning fouling indicator, but in this study, the high-pressure fouling detector more accurately captured plant fouling impacts. Finally, full-scale seawater RO plant fouling impacts were sufficiently captured while monitoring only pressure, flow and electrical conductivity; therefore, the added cost and complexity of employing more sophisticated optical, electrical, ultrasonic or other methods in *ex situ*, side stream fouling detectors may not be justified.

Keywords: Reverse osmosis; Nanofiltration; Biofouling; Seawater; Desalination; Fouling detector

1. Introduction

Algae blooms are a particular concern for seawater desalination plants due to the high concentration of algal biomass and dissolved organics present in feed water [1,2]. In particular, dissolved organics produced by algae blooms can pass through media and membrane filtration pretreatment units and induce rapid bacterial growth and biofouling of RO membranes, which increases operating pressure as well as process downtime, chemical costs and membrane degradation related to cleaning; in extreme cases, algae blooms can cause plant shutdowns [3,4]. At seawater RO

* Corresponding author.

plants, a range of influent water quality parameters have been monitored as indicators of an algae bloom (e.g., phytoplankton count, chlorophyll, phycoerythrin, dissolved oxygen, and turbidity) and those that might trigger bacterial biogrowth and biofouling (temperature, nitrate, nitrite, ammonium, phosphorous, and silica) [5]; some studies are beginning to explore the use of remote satellite imagery in combination with influent water quality parameters like chlorophyll-a [5]. Regardless, influent water quality and remote imaging can only indicate that an algae bloom is happening or, for another reason, a change in water quality has occurred, but these measures give no indication of the RO plant's response to their presence. Hence, some form of *in situ* or *ex situ* early warning fouling detection would be extremely helpful to plant operators for making appropriate operational adjustments.

Fouling detection in full-scale NF and RO membrane plants remains predominantly monitored using plant-scale key performance indicators (KPIs) such as permeate conductivity, permeate flux, feed pressure, normalized flux (=permeate flux/feed pressure), and feed-to-brine differential pressure (=feed pressure – brine pressure). While these are the KPIs of the whole plant performance, they are often slow to change and give no early warning of the onset of biofouling. One approach to achieve early warning detection was implemented by Tharamapalan et al. [6] and Tharamapalan & Duranceau [7] who installed 4 in diameter by 40-inch long ("4040") spiral wound elements in a side stream configuration to operate as the RO analog of the proverbial "canary in a coal mine" and termed a canary unit. Concentrate from the second stage of a full-scale RO process train served as the feed stream to the canary unit, thereby allowing the unit to provide an earlier indication of scaling so operators could intervene to protect the RO plant from loss of membrane productivity resulting from scaling. It is worth noting that the 4040 canary units monitored the same KPIs as the whole plant sensors, but at a localized scale, thus, isolating the impacts of scaling by directly processing the exiting concentrate stream.

Going a step further than monitoring basic RO plant KPIs, numerous laboratory scale devices for studying fouling have utilized direct (microscopic) observation through the membrane (DOTM) of colloidal fouling of microfiltration (MF) membranes [8], ultrasonic time-domain reflectometry (UTDR) to study scaling and fouling of RO membranes [9], and direct microscopic observation (DMO) to study microbial cell fouling of microfiltration membranes [10]. Since these early studies yielded new fundamental insights into membrane fouling and scaling, others have extended and adapted these (and other) tools into field-deployable *ex situ*, side-stream fouling detectors with some ability to provide early warning detection of the onset of fouling events.

Vrouwenvelder et al. [11] developed and patented an *ex situ* fouling detector known as the "Membrane Fouling Simulator" (MFS, Wetsus Water Institute, The Netherlands), which measures differential pressure through a mesh feed spacer filled flow channel [12]. In an early study, the MFS showed: (i) similar differential pressure drop as spiral wound membrane modules, (ii) reproducible performance, and (iii) efficacy as an early warning sensor of biological fouling. Through various related studies the authors suggest that fouling is a "spacer problem" and that flux has no impact on biological fouling in NF and RO systems with extensive pretreatment employed [13]. A recent study using the MFS units for comparing two RO systems operated in parallel employing different water types showed that biofouling trends in the MFS are similar to those as the spiral wound elements (SWEs) in the RO system [14], signifying the capability of the MFS unit as a biofouling indicator. Later, optical coherence tomography, a relatively new and advanced monitoring technique, was incorporated into the MFS to characterize the biomass *in situ* and non-destructively for NF [15] and RO [16] membranes. However, since the MFS operates at a low pressure and usually without permeation, it gives no indication of biofouling impacts on permeate flux, transmembrane pressure or permeate quality nor does it capture the effects of permeation and concentration polarization (CP) on biofilm formation and growth [17].

Along a similar time-frame, Uchymiak et al. [18] extended a laboratory-scale optical membrane module into a novel, *ex situ* scaling observation detector (EXSOD). Subsequently, they used their EXSOD system to optimize a brackish water RO pilot plant where mineral scaling was the primary performance limiting factor [19]. Over time, this laboratory research tool was further developed for lab and pilot scale research [20], patented [21], and ultimately, into a commercial side-stream fouling detector Imbrogno and Schäfer [22]. The EXSOD may be combined with feed-flow-reversal (FFR) to achieve RO recovery well above saturation for various mineral scales, while another commercial version of – high recovery RO using FFR, employs UTDR instead of optical detection [23].

Similarly, Sim et al. [17], developed a plate and frame "canary cell" fouling monitor designed to simulate the flow in a typical RO SWE. The canary cell mimics SWE feed channel dimensions, can accept mesh feed spacers, offers controllable cross-flow and flux, and was used in a series of membrane fouling studies over several years. Further, this canary cell has been coupled with complementary non-invasive detection methods such as ultrasonic time domain reflectometry, electrical impedance spectrometry, and the salt-pulse technique [17], which can offer additional real-time insights into membrane fouling and cleaning. It is not known if any of these canary cell iterations has been developed into a commercial fouling detector product.

Wang et al. [24] and Kang et al. [25] began developing lab-scale DMO tools for studying microbe and particle deposition and removal in low-pressure membrane filtration. Over the course of a decade, they extended the range of DMO systems from MF up to low-pressure NF/RO [26–28] and, eventually, to seawater RO [29]. Moreover, they developed experimental methods and predictive models to elucidate physical–chemical mechanisms governing attachment and removal of colloidal particles and microbial cells from membranes in open and mesh-spacer filled cross-flow channels [25,30]. From these studies, it was concluded that optical cells could provide exquisitely detailed information helpful in scientific studies, but optical images still needed to be coupled with conventional plant KPIs (i.e., flux, rejection, pressure) to know when performance decline begins at a local scale. Therefore, it was

hypothesized that an *ex situ*, side-stream canary cell capable of monitoring flux, rejection and pressure should be adequate to serve as a low-cost, early warning fouling detector with membranes easily removed for autopsy.

Herein, the performance of a low-pressure fouling detector (LPFD) and a high-pressure fouling detector (HPFD) was evaluated in an *ex situ* side-stream flow configuration at a ~1.1 ML/d (300,000 gal/d) seawater desalination demonstration plant. In addition, the fouling detectors were employed to directly assess the efficacy of various pre-treatment sequences Over the course of a 3-y demonstration study, a moderate amount of fouling was experienced by the plant, but an algae bloom was never encountered. To simulate an algae bloom, two different nutrients were dosed into the pretreated waters ahead of the LPFD and HPFD devices, and their responses were recorded.

2. Materials and methods

2.1. High-pressure fouling detector (HPFD)

The high-pressure fouling detector was made of 316 stainless steel material and composed of two pieces: (1) a top plate providing feed and concentrate ports and the cross-flow channel, and (2) a bottom plate containing the permeate channel and ports (Fig. 1). On the top plate, the feed port was parallel to the concentrate port each located on the opposite ends of the length of the plate. Two grooves were machined into the plate to hold the rubber o-ring gaskets that prevent leaking. The permeate port on the bottom plate is located at the center of the plate. A membrane coupon was placed between the two plates with active side facing towards the top plate. Feed spacer was placed in between the active side of the membrane and the top plate, and permeate spacer was placed in between the back side of the membrane and the bottom plate. The two plates were bolted together with 18 stainless steel screws on the edges. All of the wetted parts were made from 316 stainless steel material. Two concentric rubber o-ring gaskets sealed the flow channel. The flow channel was designed 254 mm long and 50.8 mm wide with a feed channel height of 0.7 mm, which matched the thickness of Pass 1 seawater NF membrane feed spacers from the full-scale (NF90, Dow Water Solutions, Midland, MI).

2.2. Low-pressure fouling detector (LPFD)

The low-pressure fouling detector was made of PVC material and composed of two pieces: (1) a top plate providing feed and concentrate ports, the cross-flow channel, and an optically clear view window, and (2) a smooth bottom plate piece. On the top plate, the feed port was parallel to the concentrate port each located on the opposite ends of the length of the plate. Two grooves were machined into the plate to hold the rubber o-ring gaskets that prevent leaking. The smooth bottom plate held the membrane to the top plate. A membrane coupon was placed between the two plates with active side facing towards the view window. Feed spacer was placed in between the active side of the membrane and the top plate. The LPFD did not have permeation, so the backside of the membrane was placed directly against the impermeable bottom plate. The two plates were bolted together with 6 stainless steel screws on the edges. All of the wetted parts were made of PVC. A single rubber o-ring gasket sealed the flow channel. The LPFD is shown in Fig. 2. The flow channel was designed to be 254 mm long and 50.8 mm wide with a feed channel height of 0.7 mm, which matched the thickness of the pass 1 SWNF membrane feed spacer.

2.3. Experimental set-up

The LPFD and HPFD units were installed in the field at the LBWD prototype desalination plant. The source water underwent several pretreatment processes before the desalination membranes, including trash racks at the channel intake to screen out coarse materials, 300 μm self-backwashing strainers prior to chlorination with sodium hypochlorite, and filtering through 0.1 μm microfiltration (MF) membranes (Pall Microza, East Hills, NY) (Fig. 3). Water exiting the MF filtrate tank was de-chlorinated using sodium bisulfate to achieve a chlorine residual of <0.1 mg/L. After dechlorination, the feed water passed through cartridge filters (CFs) before feeding into the membrane vessels. No anti-scalants or acid have been dosed to the NF feed water. The cartridge filters (Claris, PALL Corporation, East Hills, NY) were polypropylene with a nominal 5 μm pore size. The cartridge filters were replaced when the differential pressure across the filters reached 15 psi.

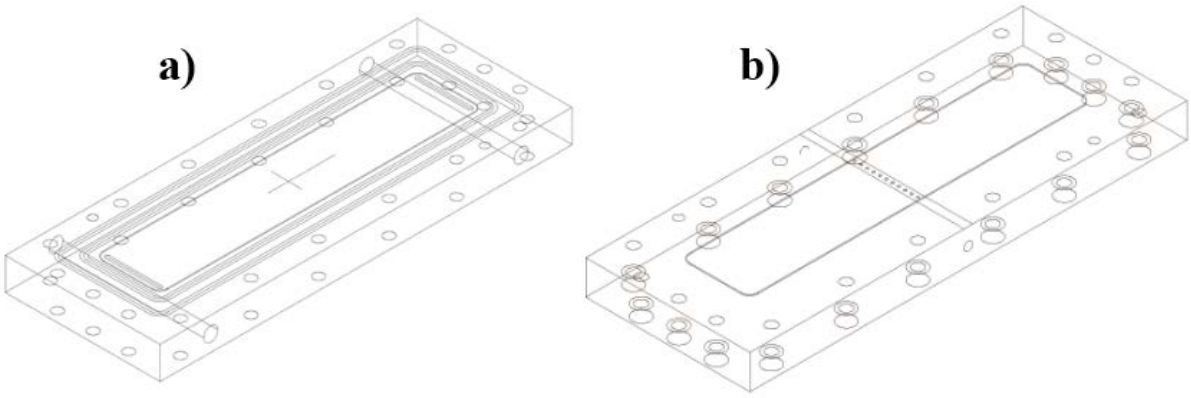

Fig. 1. Schematic of HPFD for (a) feed side and (b) permeate side.

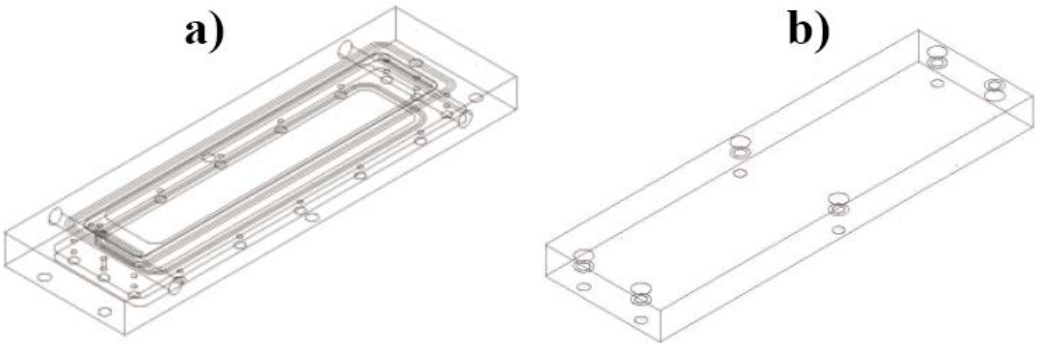

Fig. 2. Schematic of LPFD for (a) feed side and (b) permeate side.

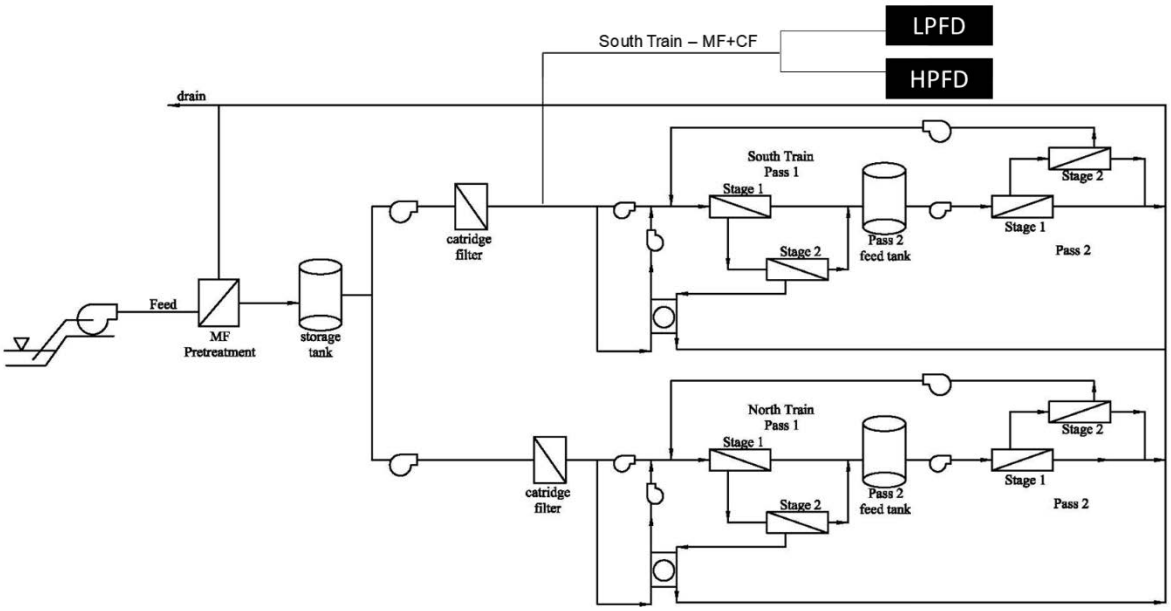

Fig. 3. Schematic of fouling detectors installing locations.

The full-scale SWNF installation consisted of 1 stage of 10 parallel pressure vessels, each pressure vessel containing 5 spiral wound membrane elements of 8 in diameter and 40 in length. The NF plant recovery was 36%. The LPFD was designed to operate at low pressure and detect membrane fouling through changes in the differential pressure (Fig. 4). Feed water from the full-scale plant entered a pressure reducing valve (Plast-O-Matic, Cedar Grove, NJ) that kept the pressure constant at 41.4 kPa (6 psi). Flexible tubing was used to connect the inlet and outlet of the detectors to a differential pressure transducer. The flow rate was controlled by a needle valve at the outlet of the detectors and monitored using a rotameter. The flow rate of the experiment was calculated so that it simulated the same Reynold's number of the prototype plant. The viewing windows of the detectors were covered with black plastic sheets to protect the membranes from exposure to sunlight.

The HPFD was operated at high-pressure, and thus, did not have a transparent viewing window (Fig. 5). Since the feed water from the MF feed tank was not at high pressure, an additional feed tank and high-pressure pump (Hydracell, Wanner Engineering, Minneapolis, NY) were needed to match the full-scale plant operating pressure. A backpressure regulator (Swagelok, Camarillo, CA) and needle valve (Swagelok, Camarillo, CA) controlled flow rate and feed pressure for each detector. Feed flowrate was measured by a hydraulic flow meter (King Instrument, Garden Grove, CA). The retentate referred to the stream after passing through either LPFD or HPFD. The permeate flow was monitored by a digital flow meter (Tovatech, South Orange, NJ).

2.4. Matching full-scale plant hydraulics in the fouling detectors

To operate the fouling detectors to simulate the full-scale plant, the Reynolds' number of the plant cross-flow was matched. Using full-size plant feed flow and number of elements, leafs per elements, and spacer thickness and porosity as inputs, the feed flow per membrane feed channel was calculated. Number of leaves per element was obtained from the autopsy described in previously submitted work [31]. This feed flow rate was the full-size plant influent split between the 2 trains, divided among the parallel spiral wound elements

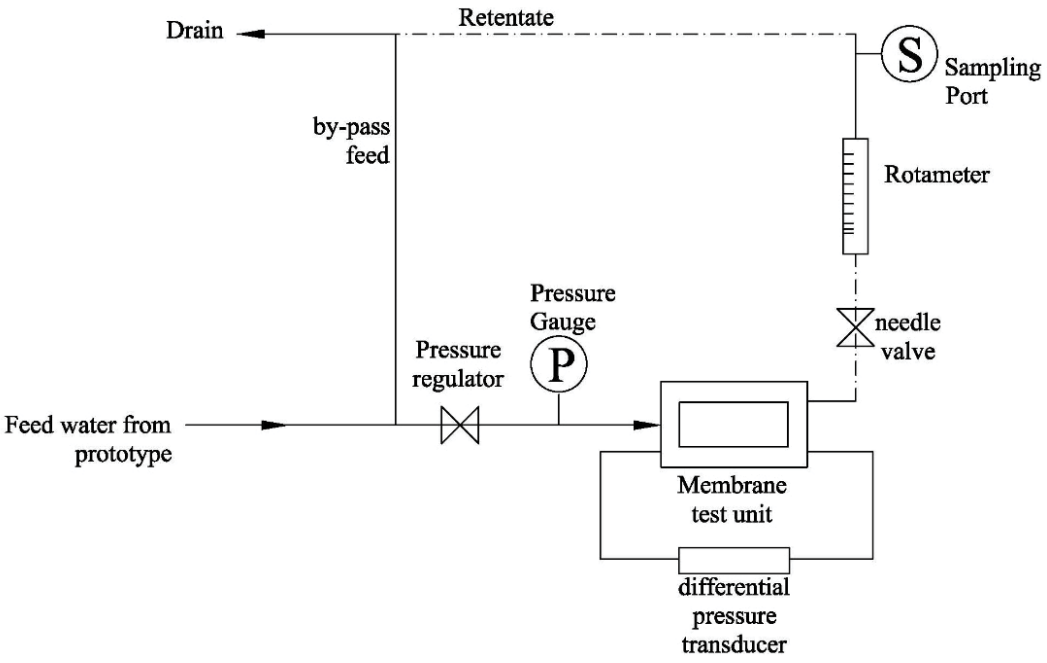

Fig. 4. Schematic of LPFD experimental set-up.

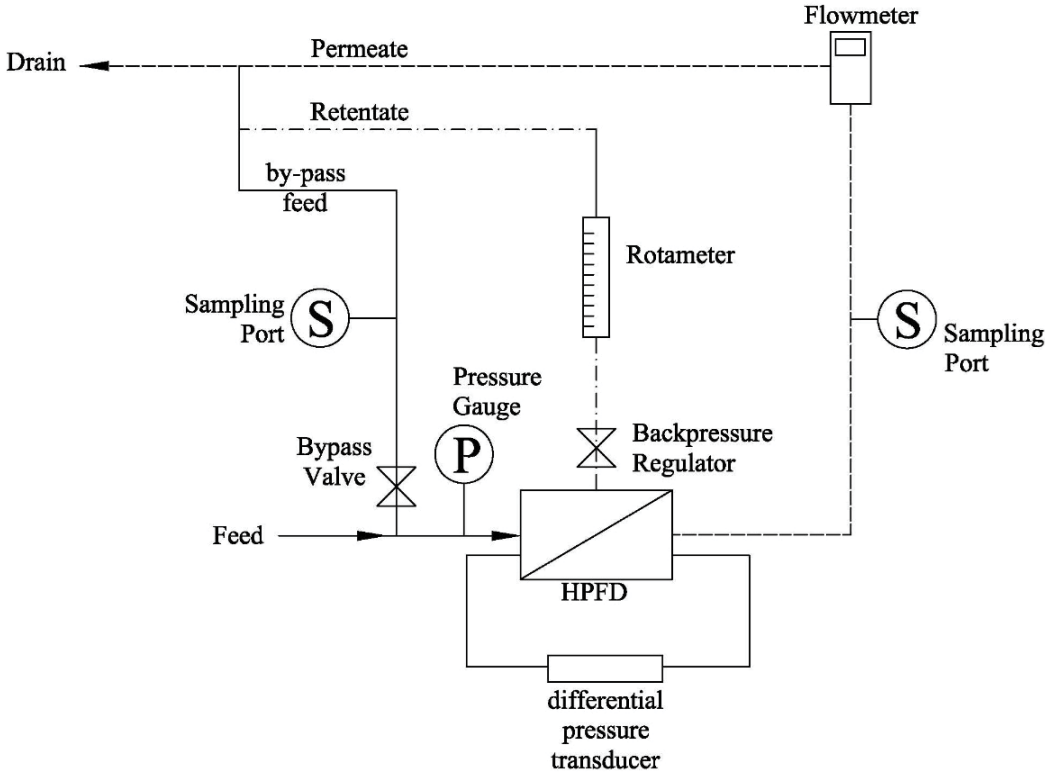

Fig. 5. Schematic of HPFD experimental set-up.

in each stack, and then, divided by the number of leaves per SWE. The operating parameters are shown in Table 1.

Channel height was defined from the total spacer thickness obtained from previously submitted work [31]. Total active area, channel length, and channel width of the membrane were measured as previously described. The actual membrane length and width minus the glue line width was taken into account. The membrane length

and width were the manufacturer's specification minus ~0.5-inches of glue line from three sides. Total active area was the actual length multiplied by the actual width. The feed spacer used in this study is non-woven geometry [32], shown in Fig. 6 and dimensions given in Table 2, with spacer porosity having a margin of error at 0.01.

Average porosity of the feed spacer was measured as follows. Several feed spacer samples of different areas were cut and each submerged in DI water in a graduated cylinder. The difference in DI water volume with and without feed spacer inside was the solid volume of the feed spacer. The void volume was the total volume of feed spacer (area × thickness) minus the solid volume. The porosity was the void volume divided by the total volume [33]. Cross sectional area of the channel, A_f was:

$$A_f = \text{channel width / channel heidht / porosity} \quad (1)$$

Cross-flow velocity of the channel in a full-scale plant was:

$$u_f = \frac{Q_f}{A_f} \quad (2)$$

Specific surface area of spacer was calculated from

$$S = \frac{4}{\text{channel height}} \quad (3)$$

hydraulic diameter was [34]:

$$d_h = \frac{4\varepsilon}{2h + S(1-\varepsilon)} \quad (4)$$

Here, Reynolds number (Re), Sherwood number (Sh), and mass transfer coefficient (k) were calculated from [34]:

$$\text{Re} = \frac{u_f d_h}{v} \quad (5)$$

$$\text{Sh} = 0.065\,\text{Re}^{0.875}\,\text{Sc}^{0.25} \quad (6)$$

$$k = \frac{\text{Sh}D}{D_h} \quad (7)$$

Active area of membrane in the fouling detectors was the length of the channel multiply by the width. Cross sectional area of the channel was:

$$A_l = \text{width / height / porosity} \quad (8)$$

Specific surface area, S and hydraulic diameter, d_h of the laboratory scale channel was the same Eqs. (3) and (4) for the full-scale but using laboratory scale dimensions.

All fouling detectors were operated at the same Reynolds number as the full-size plant's Reynolds number at the inlet side of the lead module. To calculate the necessary parameters, the following steps were taken [34]:

- Set the fouling detectors' Reynolds number to be the same as the full-size plant's lead module Reynolds number.
- Use Eqs. (6) and (7) to find Sherwood number, and mass transfer coefficient, respectively.
- Rearrange Eq. (5) to find cross-flow velocity.
- Use Eq. (2) to find the feed flow rate for the fouling detectors using channel area from Eq. (8).

Table 1
Simulator characteristics and operating conditions

Parameters	Feed flow (m^3/h)	Crossflow velocity (m/s)	Permeation velocity (mm/s)	Re	Membrane type	Feed spacer thickness
Simulation model	0.0114	0.089	0 4.0 8.0	96	NF	0.7
Prototype (lead module)	0.1535	0.102	3.8	96	NF	0.7
HPFD	0.0114	0.102	6.8	96	NF	0.7
LPFD	0.0114	0.102		96	NF	0.7

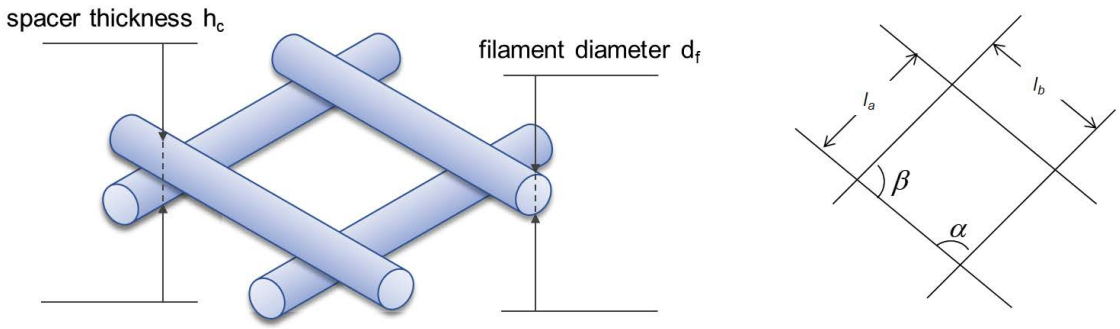

Fig. 6. Feed spacer geometry.

2.5. Evaluation of alternate pretreatments

In all cases, the influent source water underwent the pretreatment sequence described above. After dechlorination, the feed water was split into two feed tanks where each tank fed the north train and the south train. Various additional pre-treatments were explored: ultraviolet (UV) irradiation, chlorine dioxide and granular activated carbon. Ultraviolet (UV) radiation (TrojanUV, Ontario, Canada) was operated to disinfect the feed water into the north train from November 19th, 2009 until January 18th, 2010 (60 operating days). The UV radiation was operated at intensity of 31mJ/cm^2.

From October 27th, 2009 until January 18th, 2010 (54 operating days), chlorine dioxide was injected into south train. The chlorine was generated using the acid–chlorite method.

$$5NaClO_2 + 4HCl \rightarrow 4ClO_2(g) + 5NaCl + 2H_2O \quad (9)$$

The chlorine dioxide generator was built and installed by Prominent (Pittsburg, PA, USA). "Chlorine-free" chlorine dioxide (ClO_2) was expected from this method according to the manufacturer. The chlorine dioxide was added into the trains at a residual concentration of 0.5 mg/L.

After the ClO_2 addition on south train and UV radiation on north train, the feed water passed through cartridge filters (CFs) before feeding into the membrane vessels. The cartridge filters (Claris, PALL Corporation, East Hills, NY) was polypropylene material with a nominal 5 μm pore size. The cartridge filters were replaced when the differential pressure across the filters reached 15 psi.

On one of the fouling detectors, a granular activated carbon filter (GAC, PHP Micro-Carbon II, Pall Corporation, East Hills, NY) was used as an additional pretreatment in attempt to remove hydrophobic, fouling-prone organics from feed water for the bench scale experiment. Water samples were collected after each pre-treatment were collected (Table 3), and it was observed that the nutrient content of the feed water from all pretreatment yield similar nutrient content.

Table 2
Feed spacer geometry specifications

Parameter (units)	Value
Spacer thickness, h_c (μm)*	650
Filament, d_f (μm)*	325
Configuration	Diamond
l_a (mm)*	3.0
l_b (mm)*	3.0
b (°)*	90
a (°)*	90
Porosity	0.886 ± 0.010

2.6. Simulated algae blooms

The colloidal nutrient (N1) was a combination of peptone and yeast, which were selected because they are the major nutrient components of bacterial marine media [35]. Feed water was dose with a continuous concentration of 0.25 g/L peptone (Fisher Scientific, Hampton, NH) and 0.05 g/L of yeast extract (Fisher Scientific, Hampton, NH). To prepare the nutrient broth for seeding, a stock solution was mixed with DI water to contain 25 g/L peptone and 5 g/L yeast. The stock solution was sterilized by autoclaving. The stock solution was fed at 1:100 ratio with the feed water. Since the feed water was at 0.05 gpm (189 mL/min) to match the prototype's Reynold's number, the stock solution was fed at 0.0005 gpm (1.9 mL/min) so as not to significantly alter the feed flow rate into the fouling detectors.

The dissolved nutrient (N2) was a combination of sodium acetate (Fisher Scientific, Pittsburgh, PA), sodium nitrate (Fisher Scientific, Pittsburgh, PA), and sodium phosphate (Fisher Scientific, Pittsburgh, PA). The dissolved nutrient was assumed to be a representation of the dissolved nutrients in seawater. The nutrient was mixed so that the C:N:P ratio of the nutrient was 100:20:10. The nutrient solution was dosed into the feed line at 0.5 mL/min.

2.7. SEM sample preparation

Membrane samples were also imaged by scanning electron microscopy (SEM, Hitachi S-4700, Pleasanton, CA) to measure the thickness of fouling material contributed by the nutrients. Prior to the SEM analysis, dried samples were sputter-coated with a mixture of gold and palladium. Magnifications used were varied from 10,000X to 16,000X. Cross section of the membrane were cut to show the fouling thickness on the membrane surface.

2.8. Solids and ICP analyses

Membranes in fouling detectors were taken out at the end of the test for examination of solids and for ICP analyses [31]. Measurements of total and combustible solids were carried out based on Standard Method 2540D [36]. In this procedure, a section of membrane area was scraped using a sterile blade. The area of scraped membrane was measured and recorded to enable calculation of mass per unit

Table 3
Nutrient content for different types of feed water sources

	Raw seawater	MF permeate	MF+CF	MF+GAC	MF+CF+UV	MF+CF+ClO_2
TKN (mg/L)	0.267	0.236	0.238	0.270	0.248	0.282
Total P (mg/L)	0.07	0.07	0.07	0.073	0.058	0.064
TOC (mg/L)	1.069	1.018	1.488	1.675	1.408	1.668

area. The solids removed from the surface of the membrane by the blade were rinsed into ceramic dishes. The samples were then dried in the oven for 24 h at 105°C, cooled and weighed. Ceramic dishes were then placed in a furnace at 550°C for 1 h, cooled, and reweighed. The dry weight (after oven drying) gave the total solids. Total solids minus the mass of solids remaining after the furnace (non-volatile solids) gave the volatile solids.

Digested samples of extracted solids were analyzed by inductively coupled plasma optimal emission spectrometry, ICP-OES, (Model TJA Radial IRIS 1000 ICP OES, Perkin Elmer; Waltham, MA, USA) following acid digestion using HNO_3/HCl (Standard Method 3030F-Recoverable) [36]. In preparing ICP analysis, the solids were scraped from the surface of the membrane and rinsed into a 100 mL beaker. Inside the beaker, 2 mL (1:1 HNO_3) and 10 mL (1:1 HCl) were added to the suspension. The suspension was heated on a hot plate until sample was reduced to ~40 mL, making certain the water did not boil. The sample was cooled, filtered (0.45 μm membrane), and transferred to a volumetric flask where the volume was adjusted to 50 mL with deionized water. The "Multielement Standard US EPA (23 elements)" (GFS Chemicals, Powell, OH, USA) with multiple dilution (1, 5, 10, and 20 mg/L) was used to provide standards for the ICP analysis.

2.9. Biofilm density and thickness

Biofilm thickness and bacterial density on membrane surface were examined on small sections of membrane from the detectors. After drying, the stained membranes were examined under Laser Scanning Confocal Microscope (Zeiss LSM 510 META) using two excitation/emission wavelength settings, at 488/500 nm for SYTO 9 and 510/635 nm for propidium iodide. Images were captured under each excitation/emission setting. The Z sectioning method was used to determine the thickness of the biofilm. Bacterial density was evaluated by visually counting the number of cells attached to the membranes surface, and was determined by the average count number of 3 images for each sample.

3. Results

3.1. Fouling detector baseline performance

When the HPFD was operated in parallel with the full-scale plant, both permeate fluxes were calculated and compared to each other (Fig. 7a). The data show that the permeate flux for both the detector and the full-scale plant follow a similar pattern. Discrepancies in flux data were due to multiple system shutdowns in the month of March. When the experiment was restarted, the permeate flux stabilized to the same level as before. In addition, the HPFD was also capable of generating product water quality data (Fig. 7b). The permeate conductivity from the detector was compared to the south train, it became apparent that both data followed similar trends. The HPFD had slightly lower permeate conductivity than the south train since it only represented the first 10 inches of the full-scale plant where cross-flow velocity and permeate flux were highest, and hence, permeate conductivity was the lowest due to the "dilution effect".

In Fig. 7c, the differential pressures between inlet and outlet were recorded from the LPFD and HPFD simulators. A linear regression was employed to estimate the slope of the differential pressure gradients of all the pressure detectors and the full-scale plant. The data suggest that the HPFD most similarly reproduced the differential pressure gradient of the full-scale plant (0.0092 psi/d HPFD vs. 0.0141 psi/d plant). While the LPFD does not represent a full-scale plant accurately (0.0338 psi/d), it might function well as an early fouling device since it fouls sooner and more quickly than the plant, but the HPFD appears most informative as it

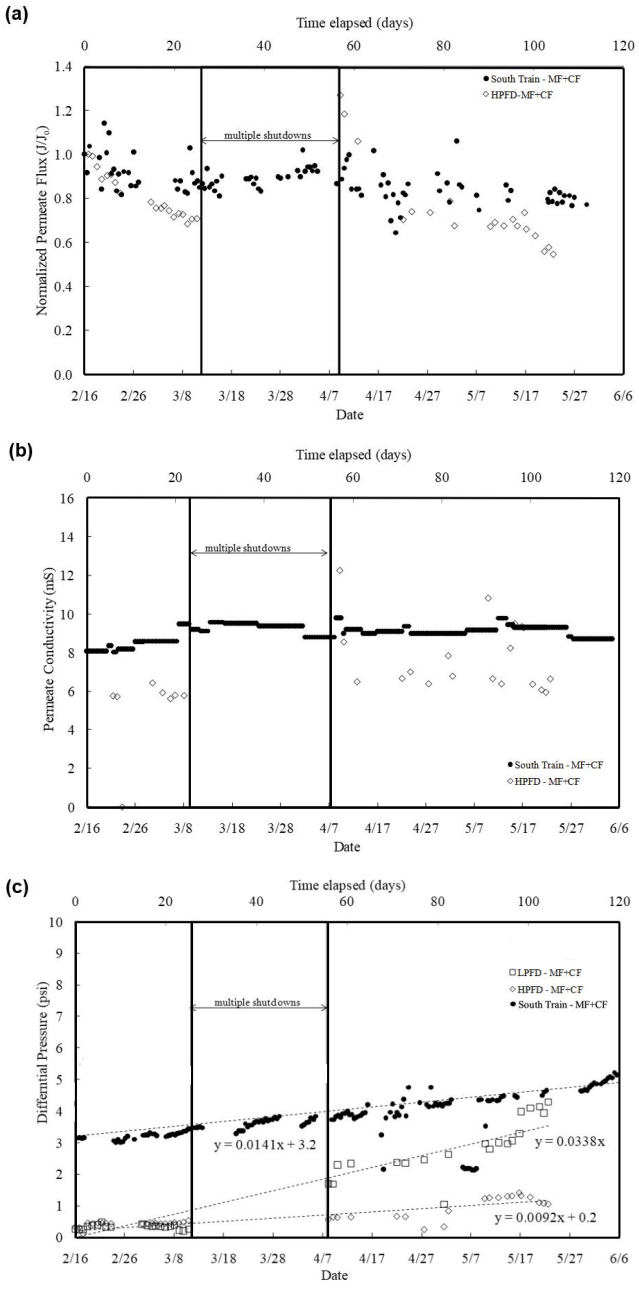

Fig. 7. Performance for baseline pre-treatment scenario for (a) permeate flux, (b) permeate conductivity, and (c) differential pressure.

reproduced four local KPIs related to flux, rejection, feed pressure and differential pressure.

3.2. Alternate pretreatment evaluation

Both south and north trains were operated in parallel with the HPFDs and the LPFDs. Since the LPFDs were without permeation, only permeate flux and permeate conductivity for HPFDs were available for comparison with plant data. Fig. 8 compares performance data from all the fouling detectors with the full-scale plant. Note, the initial permeate conductivity (Fig. 8a) for the two full-scale trains were different due to different membrane configurations inside the vessels.

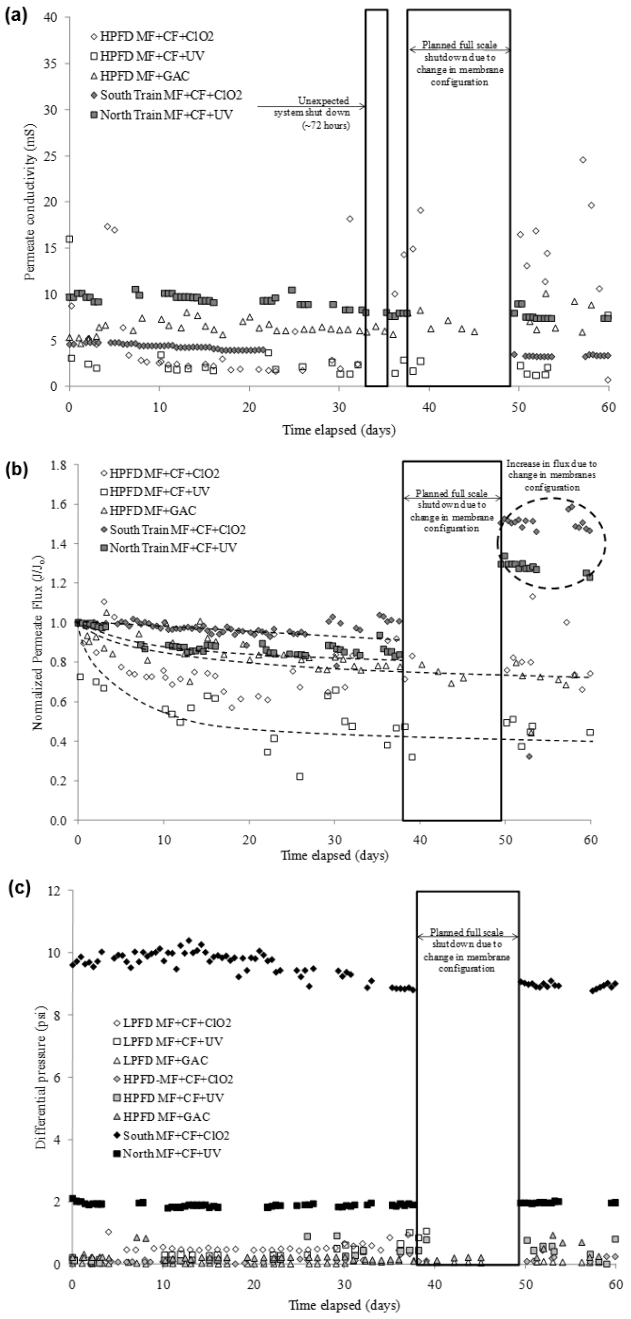

Fig. 8. Data performance vs. time for different pretreatments for (a) permeate flux, (b) permeate conductivity, and (c) differential pressure.

3.3. Performance comparison

The permeate conductivity for HPFD MF+CF+ClO_2 fluctuated about the plant values until a sudden increase after a prolonged system shut down due to mechanical malfunction. During this unexpected shutdown, feed water containing ClO_2 remained stagnant in the fouling detectors, but was flushed out of the full-scale plant. Hence, the degradation in permeate water quality was only observed in the HPFD and not in the plant. The permeate conductivity for both UV and GAC pretreated feed water remained stable and similar, but slightly better than the plant.

Both full-scale trains' performance was steady until around 12/19 when the plant was shut down to change the membrane configuration for both trains. Then, the trains were restarted on 12/28. The changes in membrane configuration increased the flux, but it was steady until the end of run time. The permeate flux for HPFD MF+CF+ClO_2 declined steadily until the plant shutdown (Fig. 8b), but jumped up dramatically about the same time the permeate conductivity increased (Fig. 8a). The increase in permeate flux further supports membrane degradation in the HPFD. However, the same membrane degradation characteristics were not observed in the full-scale plant. The permeate flux for HPFD MF+CF+UV decreased the fastest and most, while the permeate flux for HPFD MF+CF+GAC declined similarly as HPFD MF+CF+ClO_2. The water quality data reported in Table 3 also indicated that there was no significant difference in the TOC content of the water after any of the pre-treatments, so it is not clear why there were such noticeable differences in flux decline for the different pre-treatments. However, it is possible that GAC selectively removed the more fouling-prone, hydrophobic DOC fraction and ClO_2 hydrophilized DOC compounds, but all pre-treatments failed to eliminate fouling. This explained the flux decline shown for the GAC pretreated water. Overall, Fig. 8b shows that the HPFD is very sensitive to membrane degradation, which highlights the potential early warning function of this detector and also the possibility of false indications.

Fig. 8c shows the differential pressure performances for the plant, HPFD, and LPFD. The differential pressure for north train and south train was different due to different membrane configurations. However, the pattern for both trains was very similar. A slight increase in differential pressure was observed on LPFD, but there was no drastic increase observed for all pretreatment methods. No signs of membrane degradation or fouling were detected here based on the differential pressure.

3.4. Physical inspection

Fig. 9 shows the photographs for LPFD with (a) a clean membrane, (b) membrane with chlorine dioxide pretreated feed water, (c) membrane with UV radiation pretreated feed water, and (d) membrane with GAC pretreated feed water.

The membrane shown in Fig. 9a was a clean new sheet of membrane. Membranes from Fig. 9a–c were extracted after the 60 d of run time. Membranes from Fig. 9a, b and d looked the same after being extracted out of the LPFDs. The ClO_2 and GAC pre-treatments possibly oxidized or removed colored (*typ*., conjugated aromatic structures) DOC leaving only transparent extracellular polymeric (TEP) compounds commonly observed in seawater [28]. Another possibility to explain the orange color of UV pre-treated membrane is iron not being affected by UV, but being oxidized and filtered after ClO_2 and retained with charged hydrophobic organics by GAC – see Solids Analysis below for more details. The difference in brightness of Fig. 9b was not because the chlorine dioxide bleached the membrane, but rather it was due to a different level of light present when the photos were taken. While the UV pre-treated membrane in did not show significant increase in differential pressure, it appeared to accumulate more colored organics (Fig. 9c), which may explain the faster rate of flux decline (Fig. 9b).

3.5. Solids analysis

Solids analysis on membrane samples extracted from the LPFD in (Fig. 10) confirm membrane exposed to UV pretreatment contained significantly more solids than the membrane exposed to GAC and ClO_2 pretreatments. Moreover, the membrane exposed to ClO_2 had less than half of the solids than the membrane exposed to GAC pre-treatment; both having <20% of the solid mass of the UV pre-treated membrane. However, the potential for membrane degradation by ClO_2 should be taken into consideration in selection of pre-treatments. ICP analysis indicated that all fouling material on the membrane surface have similar combination of elements for the three pretreatments (Fig. 11). However, the feed water that has been exposed to UV radiation additionally contained chromium and iron. This confirms the results of the solids analysis, which showed higher concentration of inorganic solids (non-volatilized) than the organic solids.

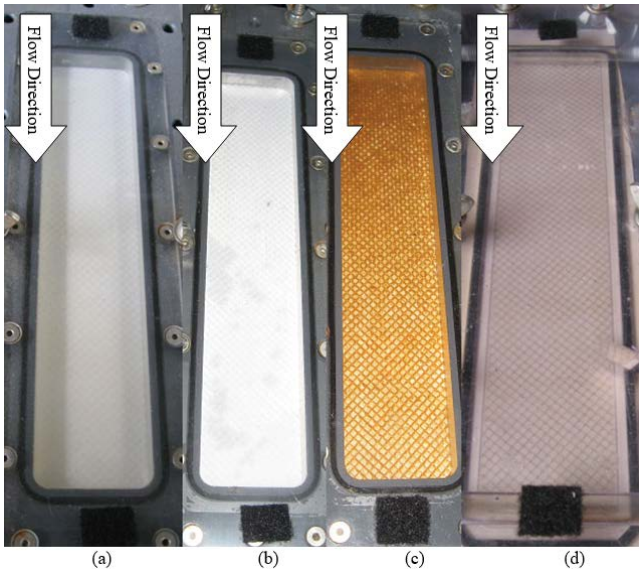

Fig. 9. Photographs of before and after use for (a) clean new membrane at day 1, (b) LPFD MF+CF+ClO_2 at final day, (c) LPFD MF+CF+UV at day 60, and (d) LPFD MF+GAC at day 60.

3.6. Simulated algae bloom results

3.6.1. LPFD differential pressure data

Fig. 12 shows differential pressure vs. time for the colloidal (N1) and dissolved (N2). The differential pressure for the low-pressure detectors exposed to the two nutrients increased faster than the low-pressure detectors without nutrient addition, which suggests fouling was stimulated by nutrient addition. The fouling detectors with nutrients added reached a differential pressure of 6 psi in 7–10 d, whereas the fouling detectors without nutrient addition took 40 d to reach 6 psi differential pressure. The colloidal nutrient stimulated fouling faster than the dissolved nutrient. It is possible that the colloidal nutrient accumulated on or around the feed spacers leading to abiotic increase in differential pressure (i.e., "spacer clogging"). Full-scale data in Fig. 12 a suggest about 2 psi increase in differential pressure over the same time period (no artificial nutrients were added to the plant feed). The 6 and 2 psi increase in the LPFD and full-scale plant differential pressures were 1.1% and 0.36%, respectively, of the initial applied pressure (550 psi). This suggests that nearly 99% of the feed pressure increase observed in the plant was due to foulant accumulation on the membrane and increased trans-membrane (hydraulic and/or osmotic) pressure.

The HPFDs did not show a significant change in differential pressure (Fig. 12b). Therefore, the low-pressure detectors might have responded to a type of fouling that did not occur as fast (or at all) when there was flux through the membrane (i.e., in both the HPFDs and the full-scale plant). The HPFD MF+CF+N2 experiment was allowed to run longer than the fouled LPFD to evaluate if the differential pressure would increase, but after 25 d no increase was observed. One should not conclude universally that seawater RO membrane fouling is only influenced by biofilm formation directly on the membranes. In a different water

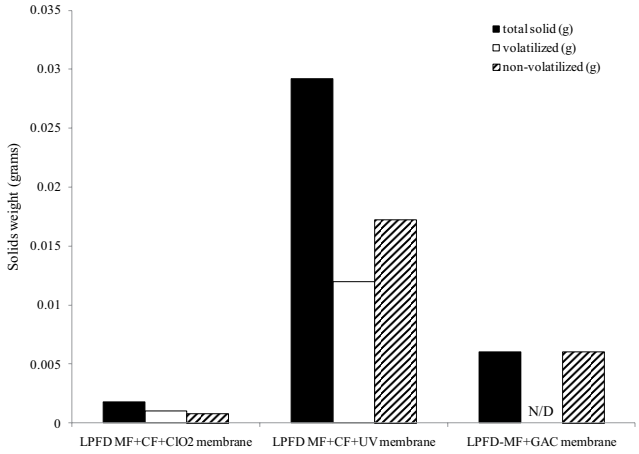

Fig. 10. Solids analyses from LPFD for different types of pretreatments.

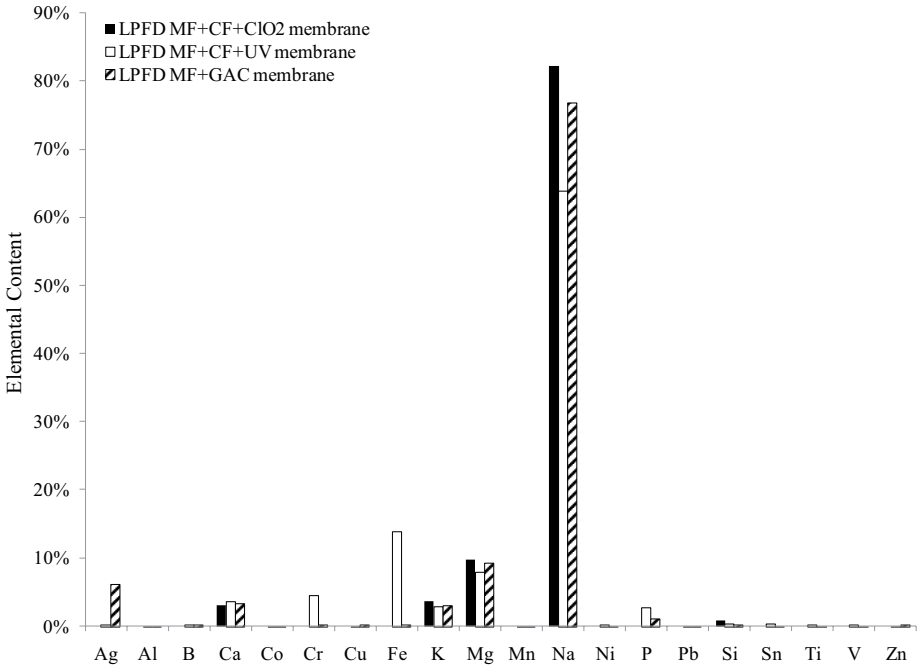

Fig. 11. ICP analysis for different types of pretreatments.

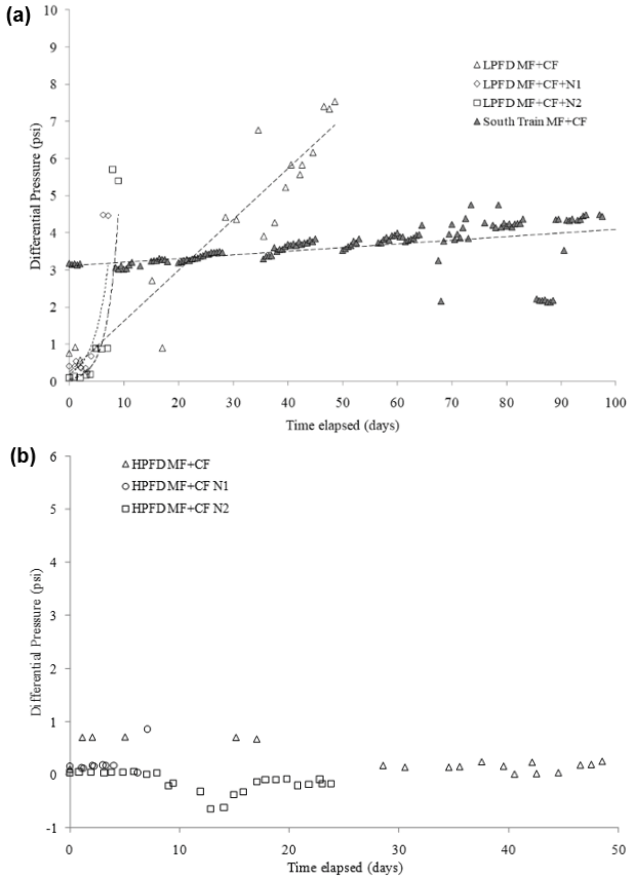

Fig. 12. Differential pressure vs. time elapsed with colloidal nutrient (N1) and dissolved nutrient (N2) addition for (a) LPFD and south train and (b) HPFD.

source with different bacteria, nutrients, membranes and spacers, it is entirely possible that an increase in differential pressure due to spacer clogging could be a significant source of flux decline.

3.6.2. HPFD performance data

In the HPFD's, salt rejection and permeate flux data was available continuously over the course of the nutrient dosing experiment. The south train of the full-scale plant experienced very little flux decline and stable rejection, while the HPFDs with and without nutrients exhibited significant, but varied extents of flux decline and some changes in rejection over the same period (Fig. 13). The HPFD operating without artificial nutrient addition experienced a much faster rate of flux decline than the full-scale plant because the actual flux through the HPFD membrane was 50% higher than the average flux of the full-scale plant. Highly permeable NF/RO membranes may not exhibit system wide flux decline even when fouling is ongoing for several months [37]. As fouling progresses, more water permeates elements further down the system and the high permeability allows the system average flux (and overall recovery) to appear constant [38]. However, in the HPFD there is only a small amount of membrane area operating at a relatively high flux. In fact, the HPFD was designed to simulate the first 10–12-inch of the full-scale system where flux and fouling are expected to be most severe and the HPFD appears to operate as designed serving well as an early warning indicator of the onset of fouling.

The colloidal nutrient produced 80% flux decline and the rejection decreased from ~90% to ~80% in only ~7 d in the HPFDs (Fig. 13). According to the solution diffusion

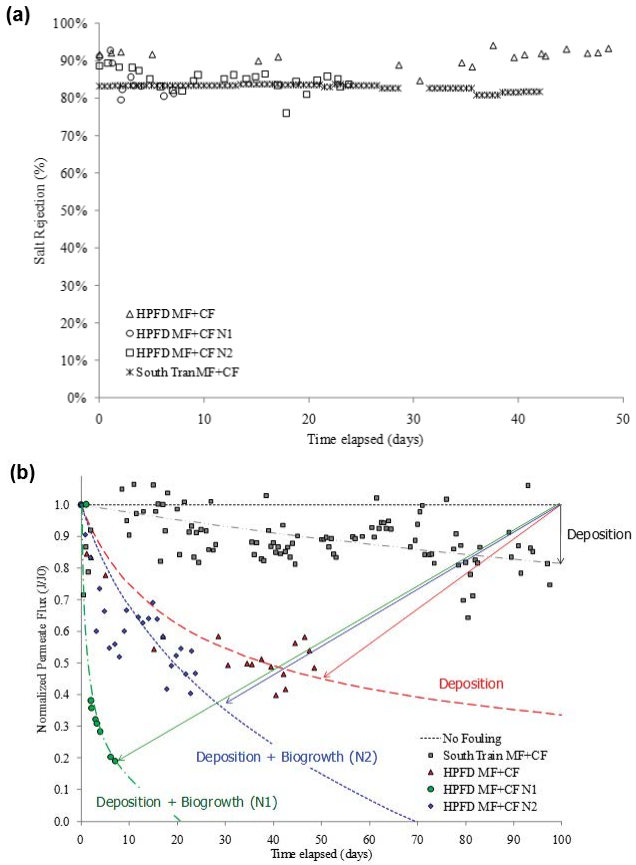

Fig. 13. (a) Salt rejection vs. time elapsed for HPFD with N1 and N2 compared to the South Train of the full-scale plant. (b) Normalized permeate flux vs. time for HPFD, HPFD with nutrients N1 and N2, and the South Train of the full-scale plant. Note the lines are eye guides only.

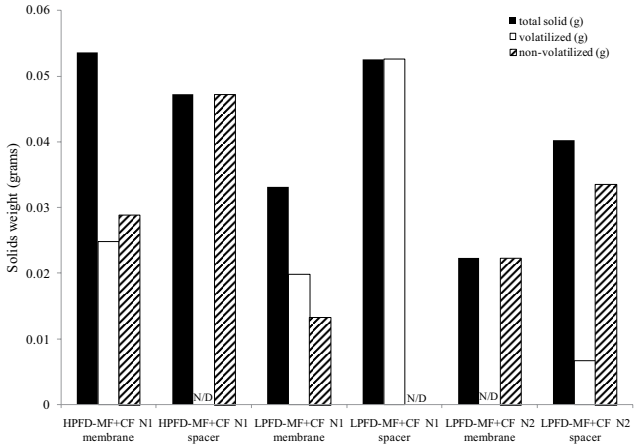

Fig. 14. Solids analysis for nutrient 1 and nutrient 2 addition.

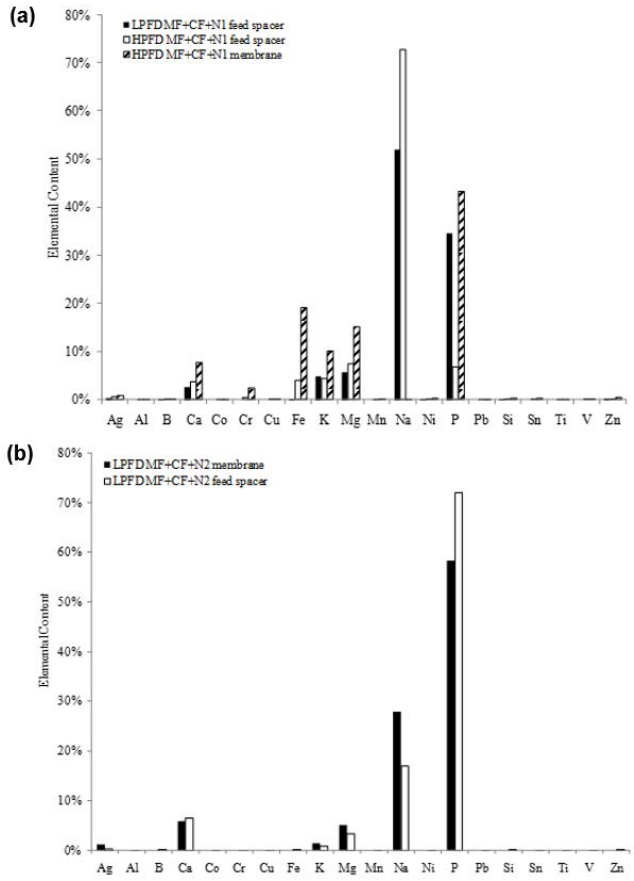

Fig. 15. ICP analysis for (a) nutrient 1 addition and (b) nutrient 2 addition.

theory, a 10% and 20% decrease in flux should decrease the salt rejection from the initial value of 83% to 81.5% and 79.6%, respectively. However, since the rejection did not decline, it is surmised that the fouling layer accumulating on the membrane surface plugged up microscopic membrane defects and enhanced the intrinsic rejection by the membrane [39]. Also, since salt rejection is not a particularly sensitive parameter, it may not be a good indicator of fouling.

Flux decline was much steeper in the HPFD dosed with colloidal nutrients than in the HPFD dosed with dissolved nutrients. Based on the full-scale data, 20% flux decline was observed within 3 months of operation (without artificial nutrient addition). Of this 20% flux decline, 0.4% was due to the increase in differential pressure; hence, the bulk of flux decline was caused by foulant accumulation directly on the membrane surface rather than clogging of the feed spacers.

3.6.3. Solids and elemental analyses

Solids accumulated on the membrane and the feed spacer during colloidal and dissolved nutrient addition experiments reveal additional insights about potential mechanisms of fouling. More total solids were found on the spacer than the membrane surface for both low-pressure detectors as shown in Fig. 14. However, more solids were observed on the membrane surface in the high-pressure detectors. In an actual spiral wound element, two membrane surfaces share a spacer and a spacer channel, thus there could be a greater distribution of foulant mass

on the membrane surface rather than on the spacers. Overall, the HPFDs mimicked the full-scale plant behavior more completely and more accurately than the LPFDs.

The ICP analyses, Fig. 15, confirmed that the chemical composition of solids found on the membrane surfaces were consistent for both colloidal and dissolved nutrients. This means that both nutrients gave rise to fouling layers of similar chemical compositions despite differences in the physical-chemical properties of the nutrients themselves. Higher concentrations of iron were found in HPFDs than in LPFDs. It's possible that the 316 stainless steel materials and/or fittings used to construct the HPFDs were corroded by seawater over the course of the experiments. Rust particles could have leached into the feed water and deposited onto the membrane surface.

3.6.4. Biofilm analyses

Electron microscopy was performed on membrane coupons extracted from the fouling detectors (Fig. 16). A dehydrated biofouling layer ~5 μm thick was observed in the membrane coupon extracted from the LPFD that had been exposed to N1. A dehydrated biofouling layer with similar thickness was observed from HPFD exposed to N1. However, the fouling layer on membrane surface from the LPFD exhibited a more uniform shape than the fouling layer on membrane surface from the HPFD. The fouling layer on the surface of the membrane from the HPFD seemed to be morphologically diverse. A possible explanation is that at low pressure, certain species of bacteria may dominate the surface. For membrane coupon exposed to N2, a thinner dehydrated biofouling layer, ~2.5 μm, was formed. Moreover, no uniform cell shape was observed, suggesting that the type of nutrient impacted the amount and type of biomass that accumulated on the membrane.

Fig. 17 shows the live and dead staining analyses done on the membrane surfaces extracted from the LPFDs and HPFDs for the colloidal nutrient and dissolved nutrient additions. The biofilm thickness found on the membrane surface in the LPFD exposed to colloidal nutrient (LPFD MF+CF+N1) was 60 μm, in the HPFD exposed to colloidal nutrient (HPFD MF+CF+N1) was 50 μm, and in the LPFD exposed to dissolved nutrient (LPFD MF+CF+N2) was 60 μm. The fouling thickness reported in the SEM analysis

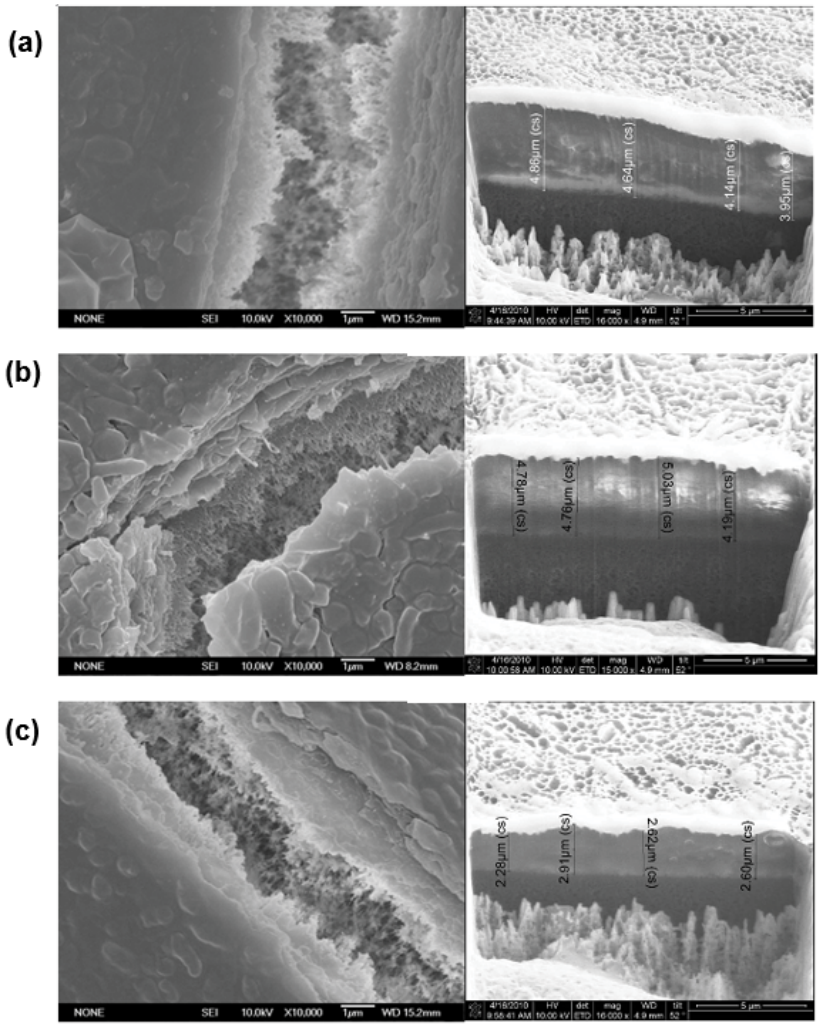

Fig. 16. SEM analysis for (a) HPFD MF+CF+N1, (b) LPFD MF+CF+N1, and (c) LPFD MF+CF+N2.

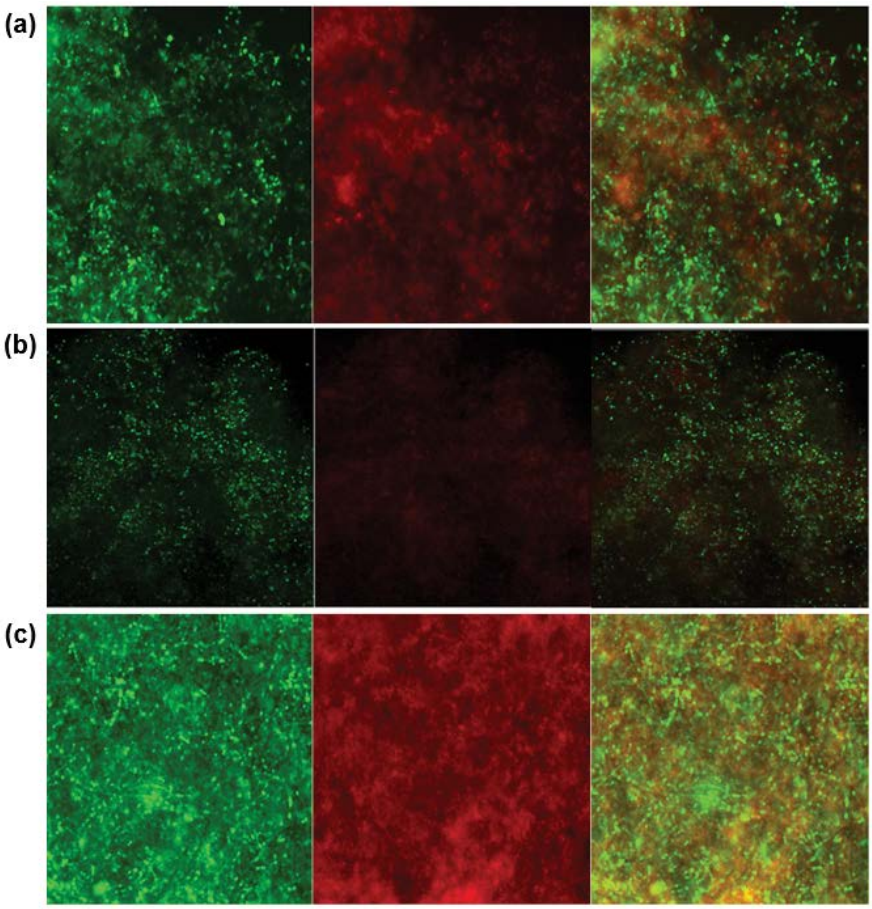

Fig. 17. Live (left), dead (middle) and combined (right) fluorescence microscopy images for membranes from (a) HPFD MF+CF+N1, (b) LPFD MF+CF+N1, and (c) LPFD MF+CF+N2.

was an order of magnitude less than the hydrated biofilm thicknesses measured by confocal laser microscopy. This is mainly due to dehydration, but SEM sample preparation, which involved dehydrating samples followed by sputter coating, could also have modified the visual appearance of biofilms. The results of cell staining analyses suggest similar amounts of live and dead bacteria on all membrane samples.

4. Discussion

In this study, the baseline performance of custom-built LPFDs (cross-flow without permeation) and HPFDs (cross-flow with permeation) was evaluated, operating in parallel on pre-treated feedwater at a full-scale seawater RO desalination plant. The baseline pre-treatment included chlorination, 0.1 μm microfiltration, dichlorination and 1 μm cartridge filter. The LPFD was capable of monitoring feed-to-brine differential pressure. The LPFD differential pressure rose faster than the full-scale plant. The main difference was the channel height and mesh spacer employed; spacer clogging occurred more quickly in the LPFD with its slightly lower channel height and thinner mesh feed spacer. Since the LPFD differential pressure was more sensitive than the full-scale plant, it could serve as an early warning detector of membrane fouling. The HPFD data reproduced the permeate conductivity and differential pressure of the full-scale plant quite reasonably, while permeate flux declined ~3X faster than the full-scale plant; hence, the HPFD could serve as an early warning fouling detector through permeate flux monitoring as well as a means of evaluating membrane integrity (e.g., via chlorine or cleaning chemical degradation) by monitoring permeate conductivity.

Next, using the LPFDs and HPFDs, four different pre-treatment sequences were assessed, including the baseline and the baseline plus UV, ClO_2 or GAC. Based on acquired performance data, physical inspection and solids analyses, ClO_2 and GAC pre-treatments were most effective at fouling control while UV added no value over the baseline. The LPFD did not give any indication of fouling through monitoring differential pressure; however, its optically transparent viewing window enabled visual verification (in real-time) that fouling occurred on membrane and spacer surfaces. An additional benefit of the high-pressure fouling detectors was that they were sensitive enough to detect both membrane fouling (flux decline) and membrane degradation (flux increase, rejection decline). Membrane degradation could be observed faster in the HPFD compared to the full-scale plant. Therefore, again the HPFD served as an early warning indicator of both membrane damage and

membrane fouling. While ClO_2 worked well in this study, autopsied membranes did show signs of chlorine damage and slight degradation. Possible causes of membrane damage include prolonged exposure to stagnant ClO_2 dosed feedwater during plant shutdowns, excess free chlorine in the potable water feeding into the chlorine dioxide generator, or components of seawater (e.g., Cl^-, Br^-, etc.) that could be oxidized and damage the membranes.

Last, the impacts of colloidal (N1) and dissolved (N2) nutrients on flux, rejection, and differential pressure were evaluated using the HPFDs and LPFDs. In LPFDs, both nutrients produced rapid increase in differential pressure within 24–48 h. In HPFDs, the nutrients produced 60%–80% flux decline within 10 to 20 d, but there was no noticeable change in salt rejection or differential pressure. These results suggest LPFDs experience foulant mass accumulation in the feed spacers, while HPFDs experience more fouling mass accumulated on the membrane surface, which may be more representative of what happens in the full-scale plant. Electron and confocal microscopy analyses confirmed that more fouling mass was found on membrane surfaces exposed to colloidal nutrients than the dissolved nutrients, suggesting colloidal nutrients may have fouled the membranes directly by convective deposition as well as indirectly by stimulating bio-growth and biofilm formation. Nutrient addition was done for a very specific concentration and ratio. For future research, it would be beneficial to research the impacts of difference in nutrient concentrations and ratios on biofilm formation and biofouling related performance decline.

Acknowledgements

Financial support for this work was provided by Long Beach Water Department, the UCLA Samueli Engineering School, the UCLA Department of Civil & Environmental Engineering, and the UCLA Sustainable LA Grand Challenge. In addition, we are grateful to (a) Dow Water Solutions for supplying NF90 membrane samples, (b) Fred Oseguera from the UCLA School of Engineering and Applied Science (SEAS) machine shop and Ray Stiver from Long Beach Water Department machine shop for their help in constructing the fouling detectors, (c) Miguel Naranjo from Long Beach Water Department for his help in installing the fouling detectors on the desalination prototype, and (d) Long Beach Water Department for providing operating data from the prototype desalination system. Last, we thank Hans Vrouwenvelder for many valuable discussions about membrane biofouling.

References

[1] E.M.V. Hoek, D. Jassby, R.B. Kaner, J. Wu, J. Wang, Y. Liu, U. Rao, Sustainable Desalination and Water Reuse, Morgan & Claypool Publishers, San Rafael, California (USA), 2021.
[2] E.M.V. Hoek, T.M. Weigand, A. Edalat, Reverse osmosis membrane biofouling: causes, consequences and countermeasures, npj Clean Water, 5 (2022) 45, doi: 10.1038/s41545-022-00183-0.
[3] M. Petry, M.A. Sanz, C. Langlais, V. Bonnelye, J.-P. Durand, D. Guevara, W.M. Nardes, C.H. Saemi, The El Coloso (Chile) reverse osmosis plant, Desalination, 203 (2007) 141–152.
[4] D.A. Caron, M.-È. Garneau, E. Seubert, M.D.A. Howard, L. Darjany, A. Schnetzer, I. Cetinić, G. Filteau, P. Lauri, B. Jones, Harmful algae and their potential impacts on desalination operations off southern California, Water Res., 44 (2010) 385–416.
[5] M.N. Gomaaa, M.A. Al-Hazmic, H.E. Mohamedd, D.J. Mullae, I. Hannachid, K.M. Sheikhof, A.M. Abouwardad, E.A.H. Mostafad, W.W. Carmichaelg, A model to predict HAB occurrence near desalination plants in the Red Sea, Desal. Water Treat., 129 (2018) 1–13.
[6] J. Tharamapalan, C.C. Boyd, S.J. Duranceau, 3-Step approach towards evaluation and elimination of acid use in pretreatment for a brackish water reverse osmosis process, J. Environ. Manage., 124 (2013) 115–120.
[7] J. Tharamapalan, S.J. Duranceau, Canary in a membrane plant: a sentinel against membrane scaling, J. Am. Water Works Assn., 106 (2014) E67–E75.
[8] H. Li, A.G. Fane, H.G.L. Coster, S. Vigneswaran, Direct observation of particle deposition on the membrane surface during crossflow microfiltration, J. Membr. Sci., 149 (1998) 83–97.
[9] A.P. Mairal, A.R. Greenberg, W.B. Krantz, L.J. Bond, Real-time measurement of inorganic fouling of RO desalination membranes using ultrasonic time-domain reflectometry, J. Membr. Sci., 159 (1999) 185–196.
[10] P.M. St. John, R. Davis, N. Cady, J. Czajka, C.A. Batt, H.G. Craighead, Diffraction-based cell detection using a microcontact printed antibody grating, Anal. Chem., 70 (1998) 1108–1111.
[11] S.M.B. Leo Peter Wessels, J.S. Vrouwenvelder, J.A.M. Paassen, Device for On-line Monitoring of Membrane Fouling During a Filtration Process Comprises a Membrane Whose Edges are Clamped Between Top and Bottom Plates, Patent In, Netherlands, 2006.
[12] J.S. Vrouwenvelder, J.A.M. van Paassen, L.P. Wessels, A.F. van Dama, S.M. Bakker, The membrane fouling simulator: a practical tool for fouling prediction and control, J. Membr. Sci., 281 (2006) 316–324.
[13] J.S. Vrouwenveder, J.A.M. van Paassen, J.M.C. van Agtmaal, M.C.M. van Loosdrecht, J.C. Kruithof, A critical flux to avoid biofouling of spiral wound nanofiltration and reverse osmosis membranes: fact or fiction?, J. Membr. Sci., 326 (2009) 36–44.
[14] G. Massons-Gassol, G. Gilabert-Oriol, J. Johnson, T. Arrowood, Comparing biofouling development in membrane fouling simulators and spiral-wound reverse osmosis elements using river water and municipal wastewater, Ind. Eng. Chem. Res., 56 (2017) 11628–11633.
[15] L. Fortunato, T. Leiknes, *In situ* biofouling assessment in spacer filled channels using optical coherence tomography (OCT): 3D biofilm thickness mapping, Bioresour. Technol., 229 (2017) 231–235.
[16] S. West, M. Wagner, C. Engelke, H. Horn, Optical coherence tomography for the *in situ* three-dimensional visualization and quantification of feed spacer channel fouling in reverse osmosis membrane modules, J. Membr. Sci., 498 (2016) 345–352.
[17] S.T.V. Sim, W.B. Krantz, T.H. Chong, A.G. Fane, Online monitor for the reverse osmosis spiral wound module—development of the canary cell, Desalination, 368 (2015) 48–59.
[18] M. Uchymiak, A. Rahardianto, E. Lyster, J. Glater, Y. Cohen, A novel RO *ex situ* scale observation detector (EXSOD) for mineral scale characterization and early detection, J. Membr. Sci., 291 (2007) 86–95.
[19] M. Uchymiak, A.R. Bartman, N. Daltrophe, M. Weissman, J. Gilron, P.D. Christofides, W.J. Kaiser, Y. Cohen, Brackish water reverse osmosis (BWRO) operation in feed flow reversal mode using an *ex situ* scale observation detector (EXSOD), J. Membr. Sci., 341 (2009) 60–66.
[20] T. Lee, J.Y. Choi, Y. Cohen, Gypsum scaling propensity in semi-batch RO (SBRO) and steady-state RO with partial recycle (SSRO-PR), J. Membr. Sci., 588 (2019) 117106, doi: 10.1016/j.memsci.2019.05.030.

[21] Y. Cohen, M. Uchymiak, Method and System for Monitoring Reverse Osmosis Membranes, Patent In, United States, 2011.
[22] A. Imbrogno, A.I. Schäfer, Comparative study of nanofiltration membrane characterization devices of different dimension and configuration (cross flow and dead end), J. Membr. Sci., 585 (2019) 67–80.
[23] A.B. Schantz, B. Xiong, E. Dees, D.R. Moore, X. Yang, M. Kumar, Emerging investigators series: prospects and challenges for high-pressure reverse osmosis in minimizing concentrated waste streams, Environ. Sci.: Water Res. Technol., 4 (2018) 894–908.
[24] S. Wang, G. Guillen, E.M.V. Hoek, Direct observation of microbial adhesion to membranes, Environ. Sci. Technol., 39 (2005) 6461–6469.
[25] S. Kang, E.M.V. Hoek, H. Choi, H. Shin, Effect of membrane surface properties during the fast evaluation of cell attachment, Sep. Sci. Technol., 41 (2006) 1475–1487.
[26] S.T. Kang, A. Subramani, E.M.V. Hoek, M.A. Deshusses, M.R. Matsumoto, Direct observation of biofouling in cross-flow microfiltration: mechanisms of deposition and release, J. Membr. Sci., 244 (2004) 151–165.
[27] A. Subramani, E.M.V. Hoek, Direct observation of initial microbial deposition onto reverse osmosis and nanofiltration membranes, J. Membr. Sci., 319 (2008) 111–125.
[28] A. Subramani, X. Huang, E.M.V. Hoek, Direct observation of bacterial deposition onto clean and organic-fouled polyamide membranes, J. Colloid Interface Sci., 336 (2009) 13–20.
[29] X. Huang, G.R. Guillen, E.M.V. Hoek, A new high-pressure optical membrane module for direct observation of sea-water RO membrane fouling and cleaning, J. Membr. Sci., 364 (2010) 149–156.
[30] S. Wang, G. Guillen, E.M.V. Hoek, Direct observation of microbial adhesion to membranes, Environ. Sci. Technol., 39 (2005) 6461–6469.
[31] D. Tanuwidjaja, X. Jin, X. Huang, C. Marambio-Jones, M. Zhang, S. Jiang, R.C. Cheng, E.M.V. Hoek, Analyses of membrane fouling and cleaning in one-pass RO and two-pass NF seawater desalination systems, J. Membr. Sci., (2010) (Submitted).
[32] B. Gu, C.S. Adjiman, X.Y. Xu, The effect of feed spacer geometry on membrane performance and concentration polarisation based on 3D CFD simulations, J. Membr. Sci., 527 (2017) 78–91.
[33] J. Wu, B. Jung, A. Anvari, S. Im, M. Anderson, X. Zheng, D. Jassby, R.B. Kaner, D. Dlamini, A. Edalat, Reverse osmosis membrane compaction and embossing at ultra-high-pressure operation, Desalination, 537 (2022) 115875, doi: 10.1016/j.desal.2022.115875.
[34] G. Schock, A. Miquel, Mass transfer and pressure loss in spiral wound modules, Desalination, 64 (1987) 339–352.
[35] M. Zhang, S. Jiang, D. Tanuwidjaja, N. Voutchkov, E.M. Hoek, B.J.A. Cai, Composition and variability of biofouling organisms in seawater reverse osmosis desalination plants, Appl. Environ. Microbiol., 77 (2011) 4390–4398.
[36] L.S. Clesceri, A.E. Greenberg, A.D. Eaton, M.A.H. Franson, American Public Health Association, American Water Works Association, Water Environment Federation, Standard Methods for the Examination of Water and Wastewater, 20th ed., American Public Health Association, Washington, D.C., 1998.
[37] K.L. Chen, L.F. Song, S.L. Ong, W.J. Ng, The development of membrane fouling in full-scale RO processes, J. Membr. Sci., 232 (2004) 63–72.
[38] E.M.V. Hoek, J. Allred, T. Knoell, B.-H. Jeong, Modeling the effects of fouling on full-scale reverse osmosis processes, J. Membr. Sci., 314 (2008) 33–49.
[39] S. Kim, S. Lee, E. Lee, S. Sarper, C.-H. Kim, J. Cho, Enhanced or reduced concentration polarization by membrane fouling in seawater reverse osmosis (SWRO) processes, Desalination, 247 (2009) 162–168.